Soils and Rocks
An International Journal of Geotechnical and Geoenvironmental Engineering
www.soilsandrocks.com
ISSN 1980-9743
ISSN-e 2675-5475

# Influence of anisotropic stress states on soil-structure interface behavior: a new experimental approach in a modified hollow cylinder apparatus

Sabine Gehring[1#], Hans Henning Stutz[1]

Article

**Keywords**
Interface tests
Stress anisotropy
Sand
Hollow cylinder triaxial device

**Abstract**

To determine the influence of soil-structure interface behavior on the bearing capacity and deformations of geotechnical structures, suitable testing methods capable of simulating in situ conditions are required. This article introduces a novel test method for soil-structure interface tests. A hollow cylinder triaxial device is modified to conduct interface tests with four independent control variables. This enables investigations of the influence of different anisotropic stress states on the contact shear behavior of granular material. First test results on Karlsruhe fine sand are presented with a variation of the lateral normal stresses acting on the plane orthogonal to the shear (i.e., contact) plane. These tests are conducted in two modes: in mode A long samples ($d_o = h$) are used whereas in mode B short samples $\left(2\left(d_o - d_i\right) = 1/h\right)$ are used. The results of the test series in mode A show that the failure occurs either in the soil (on the plane with the highest ratio of the shear and normal component of the stress vector $\tau / \sigma_N$) or on the contact plane (where the shear strength is reduced). The failure in the test series with mode B is restricted to the horizontal plane due to sample geometry. The findings will be utilized in the future to test and develop various modeling methods for soil-structure interfaces.

## 1. Introduction

To determine the loading capacity and serviceability of a geotechnical structure, the shear strength and stiffness of the soil must be tested. Many projects include rigid structures such as piles, foundations, tunnels and retaining walls (Figure 1a). In these cases, the contact shear behavior between the soil and the rigid structure is crucial to the system's behavior: For example, the surface roughness of a pile, which rules the contact shear behavior, has a major impact on its load-bearing capability (Jardine et al., 1993). Thus, a holistic understanding of the behavior of geotechnical structures requires an in-depth understanding of soil-structure interface behavior.

This inspired several authors to investigate the soil-structure contact shear behavior (e. g., Potyondy, 1961; Kishida & Uesugi, 1987; Stutz et al. 2018). The following major contributing factors have been identified: normal stress on the shear plane (Meier et al., 2023), soil density (Wernick, 1978) and ratio of the surface roughness to the grain size of soil (Uesugi & Kishida, 1986). The maximum shear stress which can be mobilized in interface tests increases with an increasing surface roughness and is limited by the soil shear strength (e.g., Kishida & Uesugi, 1987; Konkol, 2025). If the surface roughness of an interface is so high that the soil shear strength is reached in interface tests this situation is often called a fully rough interface.

These conclusions were made from test results generated in different devices for interface testing (see Figure 2). For a clear description of different boundary conditions and their influence on the sample's stress state, the following definition of the stress components of the stress tensor of the sample are used in the current work according to Figure 1b:

$$\sigma_{ij} = \begin{bmatrix} \sigma_{11} & \tau_{12} & \tau_{31} \\ \tau_{12} & \sigma_{22} & \tau_{32} \\ \tau_{13} & \tau_{23} & \sigma_{33} \end{bmatrix} = \begin{bmatrix} \sigma_{PP} & \tau_{12} & \tau_{31} \\ \tau_{12} & \sigma_{OP,1} & 0 \\ \tau_{13} & 0 & \sigma_{OP,2} \end{bmatrix} \quad (1)$$

$\sigma_{PP}$ is the normal stress on the plane parallel to the contact surface. The orthogonal planes are chosen such that there is no shear stress $\tau_{23}$ and the normal stress components on these planes are called $\sigma_{OP,1}$ and $\sigma_{OP,2}$.

Most of the laboratory interface tests are conducted using modified direct shear tests (Figure 2a, e.g., Potyondy, 1961; Frost & Han, 1999; Stutz & Martinez, 2021) or simple shear test devices (Figure 2b, e.g., Kishida & Uesugi, 1987). In these tests (as well as in modified ring shear tests, Figure 2c,

#Corresponding author. E-mail address: sabine.gehring@kit.edu
[1]Karlsruher Institut für Technologie, Institut für Bodenmechanik und Felsmechanik, Karlsruhe, Germany.

Submitted on February 21, 2025; Final Acceptance on September 19, 2025; Discussion open until February 28, 2026.
Editor: Renato P. Cunha
https://doi.org/10.28927/SR.2025.003725

e.g., Lemos & Vaughan, 2000), different boundary conditions are applied on the plane parallel to the contact plane ("parallel plane" in Figure 1b). For example, the stress component $\sigma_{PP}$ of the stress tensor in the sample (see Equation 1 and Figure 1b) can be controlled. On the "orthogonal planes" (Figure 1b), the deformation is restricted by the frames or stacked rings in the devices. Thus, the stress components $\sigma_{OP,1}$ and $\sigma_{OP,2}$ of the tensor cannot be controlled and are unknown. Because of those test boundary conditions, information regarding the impact of various boundary conditions on the orthogonal plane is scarce. First tests toward the influence of the three-dimensional stress state were conducted by Corfdir et al. (2004). They developed a new test device and controlled one normal stress component $\sigma_{OP,1}$ on an orthogonal plane in the sample in addition to the normal stress component $\sigma_{PP}$ on the parallel plane. Corfdir et al. (2004) used a rotating cylinder inside a hollow cylinder-shaped sample as contact plate for the interface (Figure 2d). With an annular confining cell, the normal stress on the shear plane is applied and with an axial piston, one additional normal stress $\sigma_{OP,1}$ can be controlled. Another approach by Tejchman & Wu (1995) and Liu et al. (2024) is an inclined rigid surface in a triaxial or biaxial device (see Figure 2e). In such tests, the normal stress components $\sigma_{OP,1}$ and $\sigma_{OP,2}$ on the orthogonal planes can be calculated, but however, not independently controlled.

Investigations on the influence of different stress states and the entire 3D-stress tensor on contact shear behavior are not only crucial for gaining a better understanding of interface behavior, but is also useful for evaluating different modeling methods for soil-structure interaction. In general, two different approaches to develop constitutive models for interfaces exist in the literature (see Figure 1c). The first approach uses only the stress vector on the shear plane and the relative displacement at the interface (e.g., Ghionna & Mortara, 2002; Stutz et al., 2014). Because soil shear behavior and contact shear behavior are similar, the second approach uses the idea of deriving interface models from

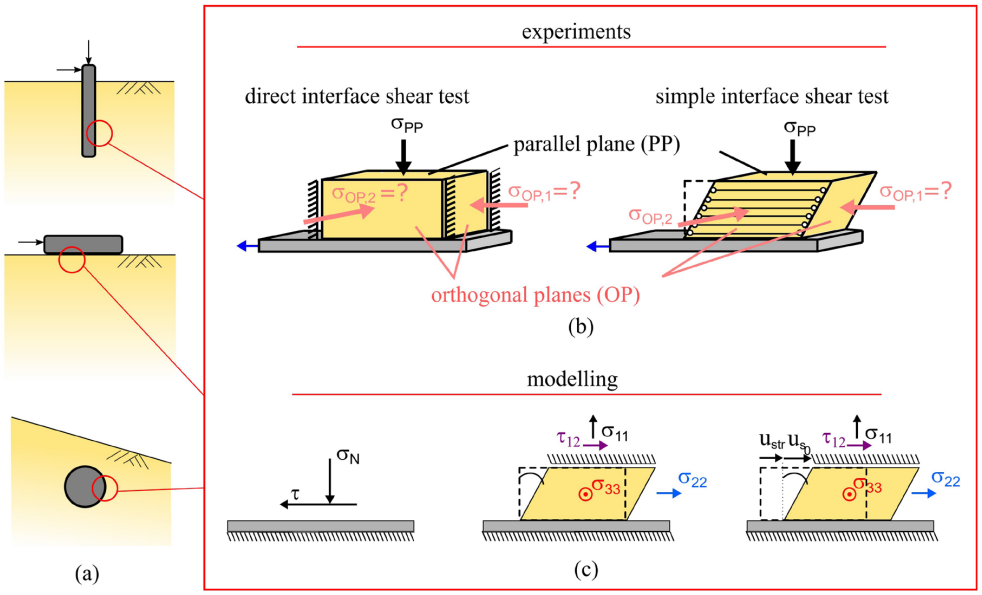


**Figure 1.** Interface shear behavior: (a) practical examples, (b) unknown stress on orthogonal plane for common interface tests, (c) modeling approaches for interface behavior.

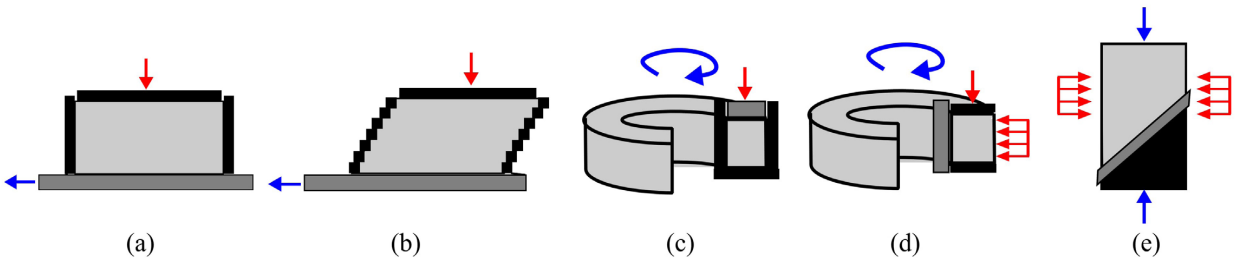


**Figure 2.** Different test setups for interface tests: (a) modified direct shear apparatus, (b) modified simple shear device, (c) modified ring shear apparatus, (d) rotating interface in sample ring and annular confining cell, (e) inclined contact surface in triaxial or biaxial device.

existing soil models by reducing the shear strength of the model (e.g., Gehring et al., 2023). This is supported by the experimental observation, that the relative displacement between contact surface and soil consists of localized shear strains in a shear band in the soil (DeJong et al., 2006). Using this method, the entire 3D stress tensor in the sample is considered. The last-mentioned approach for contact modeling is based on different assumptions concerning the stress state at the interface: equal normal stresses ($\sigma_{PP} = \sigma_{OP,1} = \sigma_{OP,2}$ , Arnold & Herle, 2006), negligible deformations at the orthogonal plane ($\sigma_{PP} \neq \sigma_{OP,1} = \sigma_{OP,2}$, Stutz et al., 2017) or a coupling with neighboring soil elements in FEM ($\sigma_{PP} \neq \sigma_{OP,1} \neq \sigma_{OP,2}$ Staubach et al., 2022). Furthermore, recent research incorporated the consideration of stick and slip conditions between the surface and the soil in combination with the second approach (Niebler et al., 2025). Thereby, the total displacement of the interface is divided into the displacement due to sliding of the contact plate $u_{str}$ and the displacement due to the shearing of the soil $u_{so}$ (see Figure 1c). To choose a suitable method and verify or contradict the existing approaches, experimental evidence with various stress states is required.

Despite these needs, data on the influence of different stress states and boundary conditions on the orthogonal plane is limited and existing methods can only control one stress component on an orthogonal plane $\sigma_{OP,1}$. Therefore, a novel test method is presented here. This method allows to control two stress components $\sigma_{OP,1}$ and $\sigma_{OP,2}$ on planes orthogonal to the shear plane. To conduct such interface tests, a hollow cylinder triaxial device is modified with a contact plate. The modified device, due to its four independent control parameters, offers diverse opportunities for interface testing with various stress states. The first test series on Karlsruhe fine sand with different stress conditions and contact plates with varying roughness properties are conducted and interpreted concerning the failure mechanism.

## 2. Materials and test setup

### 2.1 Test material (soil and surface)

The experiments were conducted on medium dense samples of Karlsruhe fine sand. A grain size distribution for Karlsruhe fine sand is shown in Figure 3a and index properties are listed in Table 1. The grain size distribution is uniformly graded. The grain shape can be characterized with an aspect ratio of 1.289 (ratio between longest length of the grain and the length orthogonal to it) and is illustrated in Figure 3b. For the sample preparation, the membranes are placed in a mold and the sand is air pluviated between the membranes (Figure 3c). A nozzle with a diameter of 4 mm is used for pluviation and is moved with a constant distance to the sample top.

The samples have an outer diameter of 100 mm, and inner diameter of 60 mm and a height of 100 mm (mode A). In the test series with short samples (mode B), the sample height is reduced to 20 mm. In the modified hollow cylinder triaxial device for interface tests, ring plates are used as contact surfaces (for the test setup see Section 2.2).

**Table 1.** Index quantities of Karlsruhe fine sand (Wichtmann & Triantafyllidis, 2016).

| | Karlsruhe fine sand |
|---|---|
| grain density $\rho_s$ | 2.65 g/cm³ |
| $e_{min}$ | 0.677 |
| $e_{max}$ | 1.054 |
| Aspect ratio | 1.289 |

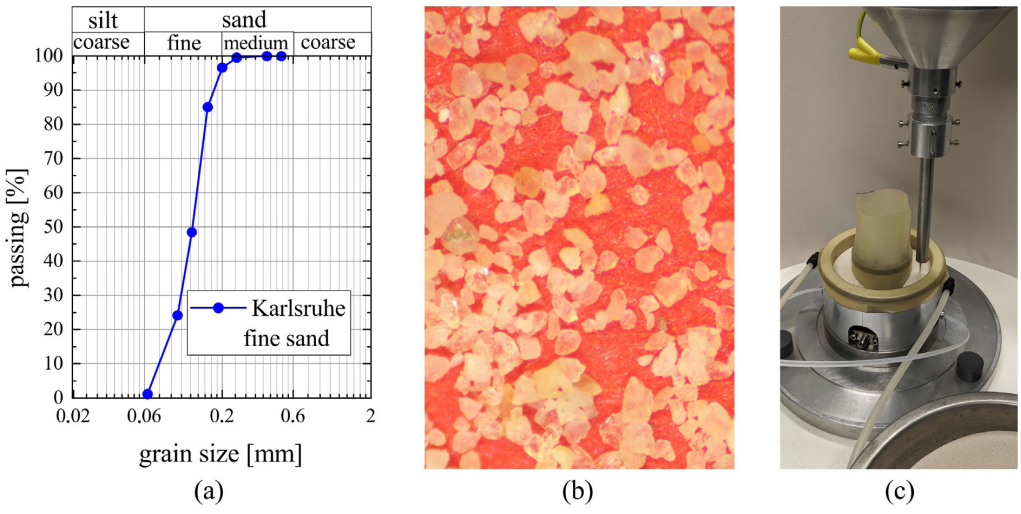


**Figure 3.** Karlsruhe fine sand (KFS). (a) grain size distribution of Karlsruhe fine sand, (b) microscopy of grains, (c) sample preparation (air pluviation) exemplary for mode B.

Steel rings with different roughness properties are used in the presented test series. They are displayed in Figure 4a, b and c and listed in Table 2.

The roughness property $R_a$ is equivalent to the center line average (CLA) and is defined as the average deviation from the mean line of the surface (see Figure 4d). It is important to mention, that the surfaces of the contact plates K1 and K3 contain two porous stones and six screws (Figure 4a). The measured roughness was obtained between the screws. K11 was developed as an improved contact plate without screws. This provides a uniform roughness across the entire contact area and is therefore consistent with the roughness measurements (Figure 4b). The roughness $R_a$ of the plates was measured with a digital microscope on three spots on the plates and averaged thereafter.

## 2.2 Test setup and procedure

In the modified hollow cylinder triaxial device, a ring-shaped sample is sheared against a contact plate by rotating the bottom plate against the top plate (see Figure 5). In common hollow cylinder triaxial tests, both end plates are fully rough and manufactured with steel fins or coarse grains (Broms & Casbarian, 1965; Hight et al., 1983). The aim is to ensure a transfer of the displacement of the end plates to the sample with nonslip traction and full mobilization of the soil strength. To conduct interface tests with this device, a changeable top plate was manufactured. In the modified device, interface tests with contact plates with different

**Table 2.** Overview of used contact plates.

| contact plate | roughness $R_a$ (excluding screws) | manufacturing of surface |
|---|---|---|
| K0 | >230µm, fully rough | glued sand grains (with screws) |
| K3 | > 0.7 µm | Fine sand blasted (with screws) |
| K11 | ≈ 0.7 µm | polished (no screws) |


**Figure 4.** Photographs of contact plates K0 (a), K3 (b) with screws and K11 (c) without screws, (d) schematic of average roughness value $R_a$.

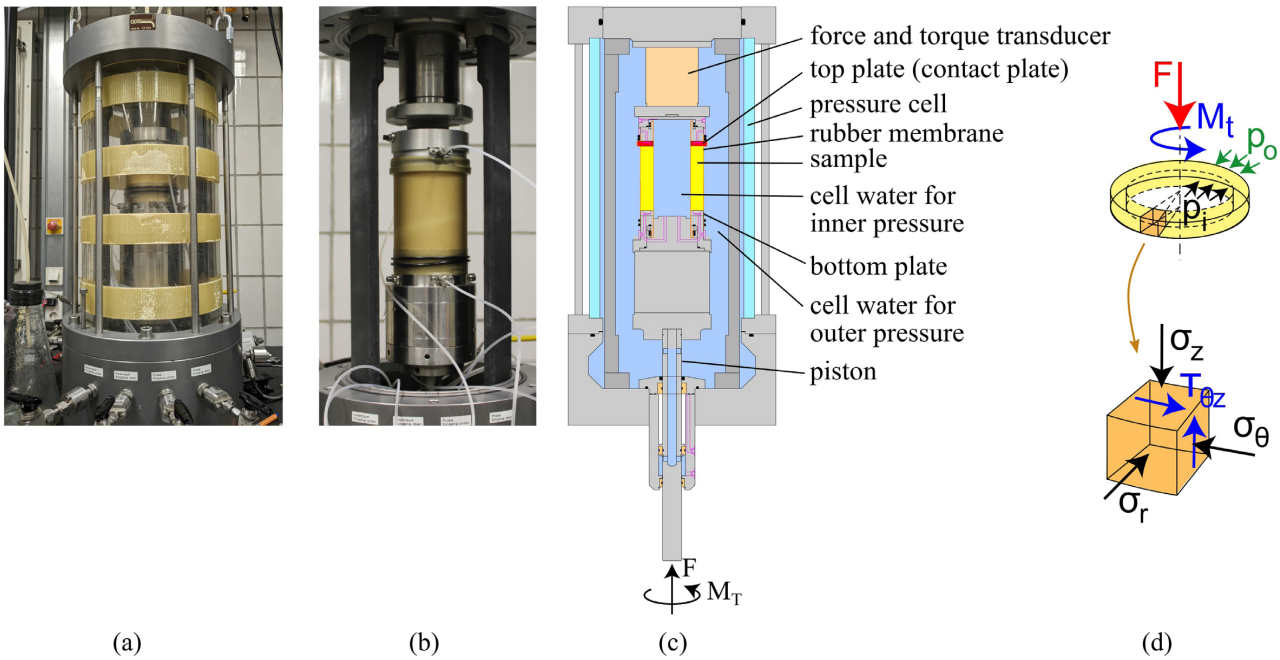


**Figure 5.** Modified hollow cylinder device for interface tests. (a) photograph of mode B with pressure cell, (b) photograph of mode A without pressure cell, (c) schematic of setup mode A, (d) loading and stress state of the sample.

roughness properties can be performed. The top plate was further enhanced with a screw-free variant (K11) to obtain a uniform surface. The sample is covered with membranes on the outer and inner surface area. The outer and inner cell water is separated, so it is possible to control four independent control parameters: the axial force or displacement, the torsional momentum or rotation, the outer cell pressure, and the inner cell pressure. Two of them are used to apply a normal stress on the shear plane (axial force) and a shear displacement to the interface (torsion). This leaves two more control parameters to control the normal stresses $\sigma_{OP,1}$ and $\sigma_{OP,2}$ on the orthogonal planes and enables studies of the interface behavior with complex stress states.

In Figure 5d a schematic soil element with the components of the stress tensor in the sample is displayed at the bottom with the globally measured forces and pressures acting on the whole sample above. The stress elements form the following stress tensor and its transfer to the stress tensor defined above the interface:

$$\sigma_{ij} = \begin{bmatrix} \sigma_z & 0 & \tau_{\theta z} \\ 0 & \sigma_r & 0 \\ \tau_{z\theta} & 0 & \sigma_\theta \end{bmatrix} = \begin{bmatrix} \sigma_{PP} & 0 & \tau_{31} \\ 0 & \sigma_{OP,1} & 0 \\ \tau_{13} & 0 & \sigma_{OP,2} \end{bmatrix} \quad (2)$$

The following equations show the relationships between the global measured values and the stress components for average stresses with the assumption of equal work of the global measured forces and the stresses acting in the sample (see Saada, 1988):

$$\sigma_z = \frac{F_{ax}}{\pi\left(r_o^2 - r_i^2\right)} + \frac{p_o r_o^2 - p_i r_i^2}{r_o^2 - r_i^2} \quad (3)$$

$$\sigma_r = \frac{p_o r_o + p_i r_i}{r_o + r_i} \quad (4)$$

$$\sigma_\theta = \frac{p_o r_o - p_i r_i}{r_o - r_i} \quad (5)$$

$$\tau_{\theta z} = \frac{3M_t}{2\pi\left(r_o^3 - r_i^3\right)} \quad (6)$$

From these stress components, the principal stresses can be calculated:

$$\sigma_1 = \frac{\sigma_z + \sigma_\theta}{2} + \sqrt{\left(\frac{\sigma_z - \sigma_\theta}{2}\right)^2 + \tau_{\theta z}^2} \quad (7)$$

$$\sigma_2 = \sigma_r, \quad (8)$$

$$\sigma_3 = \frac{\sigma_z + \sigma_\theta}{2} - \sqrt{\left(\frac{\sigma_z - \sigma_\theta}{2}\right)^2 + \tau_{\theta z}^2} \quad (9)$$

The ratio of the principal stresses is often depicted with the coefficient $b$:

$$b = \frac{\sigma_2 - \sigma_3}{\sigma_1 - \sigma_3} \quad (10)$$

The Roscoe invariants are defined as:

$$\text{mean pressure } p = \frac{1}{3}\left(\sigma_z + \sigma_r + \sigma_\theta\right) \quad (11)$$

$$\text{deviator stress } q = \sqrt{\sigma_z^2 + \sigma_r^2 + \sigma_\theta^2 - \sigma_z\sigma_r - \sigma_z\sigma_\theta - \sigma_r\sigma_\theta + 3\tau_{\theta z}^2} \quad (12)$$

$$\text{Lode angle } \theta = \cot\sqrt{3} \cdot \frac{b}{2-b} \quad (13)$$

After the sample preparation (see Section 2.1) the samples were saturated. For this purpose, the samples were first flushed with CO2, flushed with water under atmospheric pressure, then flushed with water and a backpressure of $200\,\text{kPa}$ and in the end the backpressure was increased to $500\,\text{kPa}$. The saturation was verified with a B-value greater than 0.97. After this, the samples were consolidated to the initial stress state. With an open drainage the axial force $F_{ax}$ and the outer and inner cell pressures were increased up to the desired values. The reached effective values of $\sigma_z', \sigma_r'$ and $\sigma_\theta'$ were kept constant during the test for all experiments.

All tests were conducted with the same vertical stress $\sigma_z' = \sigma_{PP}'$ of 100 kPa (normal stress on the parallel plane). The normal stresses on the orthogonal plane (radial stress $\sigma_r' = \sigma_{OP,1}'$ and tangential stress $\sigma_\theta' = \sigma_{OP,2}'$) were varied from test to test. These stresses were kept constant during the entire test. After reaching the test specific initial stress state, the drained contact shearing phase was started by rotating the bottom endplate. The bottom plate was rotated with a constant velocity of $\theta = 0.2$ deg/min. This leads to an increase of the shear stress on the horizontal plane $\tau_{\theta z}$.

## 3. Results and discussion

All tests are conducted with medium dense samples with a target relative density $I_{D,0} \approx 0.6$ after the sample preparation. The actual relative density can be found in Table 3 together with the boundary conditions of the presented tests. $I_{D,0}$ and $e_0$ represents the initial density and the void ratio directly after the sample preparation and before the consolidation.

### 3.1 Influence of membrane stiffness

During the shear phase (torsion) of the test, not only the sample is deformed but also the membranes. Since the membranes are fixed at the bottom and top caps, they are deformed due to rotation of the end plates and therefore contribute to the globally measured forces.

In test series B01:K3 and B02:K0 experiments with short samples with a height of 20 mm are conducted. Especially for these tests and a rotation of the bottom plate up to 40°, the influence of the membrane stiffness cannot be neglected: The measured moment during torsion tests results not only from the mobilized friction on the sample but also from stresses in the membrane.

In the literature, one method to correct the measured data results from the shear stress emerging from elastic membrane deformation due to torsion:

$$\tau_M = \frac{t_M E_M \left(r_o^3 + r_i^3\right)\theta}{\left(r_o^3 - r_i^3\right)h} \tag{14}$$

with the global measured shear stress due to membrane deformation $\tau_M$, the thickness $t_M$ and the elastic modulus $E_M$ of the membranes, the rotation angle $\theta$ and the height $h$ and inner $r_i$ and outer radius $r_o$ of the specimen (e.g. Koseki et al., 2005; Kiyota et al. 2008). Koseki et al. (2005) and Kiyota et al. (2008) used dummy tests with water-filled membranes to validate this relationship and to develop further correction formulas for large deformations. Especially when large deformations occur, these tests with water-filled membranes show different deformation patterns than the drained tests in the present work. Therefore, a new correction method is developed to compensate for the effect of the membrane stiffness on the test results. Tests on soil samples with different membranes (V15 and V17) are used to capture the actual membrane (or sample) deformation and a mathematical correction is developed. The following membrane types were used here:

- Latex membrane, stiffness $E_{\text{latex}} = 1387\,\text{kPa}$ , thickness $t_{\text{latex}} = 0.55$ (average of inner and outer membrane in test V15)
- Butyl membrane, stiffness $E_{\text{butyl}} = 1706\,\text{kPa}$, thickness $t_{\text{butyl}} = 0.64$ (average of inner and outer membrane in test V17)

The membrane stiffness was obtained with tension tests using dummy samples to maintain the shape of the membrane and restrict the lateral strain of the membrane. The calculated shear stress from the globally measured momentum of tests V15 and V17 is shown in Figure 6. The tangential displacement $s_t$ represents the displacement of a point on the average circumference on the bottom plate along its average circumference. The shear stress of both tests increases and reaches at approximately 5 mm tangential displacement a more shallow, linear path. The linear increase of test V17 with butyl membranes follows a steeper linear path and therefore reaches a higher shear stress. This shows a larger influence of the membrane stiffness resulting from a larger stiffness of the butyl membranes. From this difference, the stress induced by membrane deformation is calculated for these tests and transferred to a general correction function.

If the membrane deformation is similar in two tests and in the elastic range, the additional global shear stress or measured torque resulting from the membrane stiffness is proportional to the thickness and stiffness of the membranes (see Equation 14). With two different types of membrane with different thickness and stiffness, the ratio of the additional measured global shear stress can be estimated. Here, the global shear stress induced by the membrane stiffness in the test with latex membranes $\tau_M^{latex}$ and in the test with butyl membranes $\tau_M^{butyl}$ have the following relationship:

**Table 3.** Overview of presented tests.

| series | No. | mode | contact plate | $I_{D,0}$ | $e_0$ | $\sigma_z'$ | $\sigma_\theta' = \sigma_r'$ | $p'$ |
|---|---|---|---|---|---|---|---|---|
| A01:K11 | V26 | A | K11 (smooth) | 0.59 | 0.83 | 100 kPa | 50 kPa | 67 kPa |
| A01:K11 | V28 | A | K11 | 0.58 | 0.837 | 100 kPa | 100 kPa | 100 kPa |
| A01:K11 | V29 | A | K11 | 0.61 | 0.82 | 100 kPa | 150 kPa | 133 kPa |
| A01:K11 | V30 | A | K11 | 0.61 | 0.82 | 100 kPa | 150 kPa | 133 kPa |
| A02:K0 | V02 | A | K0 (rough) | 0.70 | 0.79 | 100 kPa | 100 kPa | 100 kPa |
| A02:K0 | V31 | A | K0 | 0.66 | 0.80 | 100 kPa | 150 kPa | 133 kPa |
| A02:K0 | V32 | A | K0 | 0.62 | 0.82 | 100 kPa | 50 kPa | 67 kPa |
| B01:K3 | V08 | B | K3 (less rough) | 0.62 | 0.82 | 100 kPa | 100 kPa | 100 kPa |
| B01:K3 | V09 | B | K3 | 0.63 | 0.82 | 100 kPa | 150 kPa | 133 kPa |
| B01:K3 | V10 | B | K3 | 0.63 | 0.82 | 100 kPa | 50 kPa | 67 kPa |
| B01:K3 | V21 | B | K3 | 0.56 | 0.85 | 100 kPa | 175 kPa | 150 kPa |
| B02:K0 | V15 | B | K0 (rough) | 0.76 | 0.77 | 100 kPa | 100 kPa | 100 kPa |
| B02:K0 | V18 | B | K0 | 0.49 | 0.87 | 100 kPa | 150 kPa | 133 kPa |
| B02:K0 | V20 | B | K0 | 0.65 | 0.81 | 100 kPa | 50 kPa | 67 kPa |

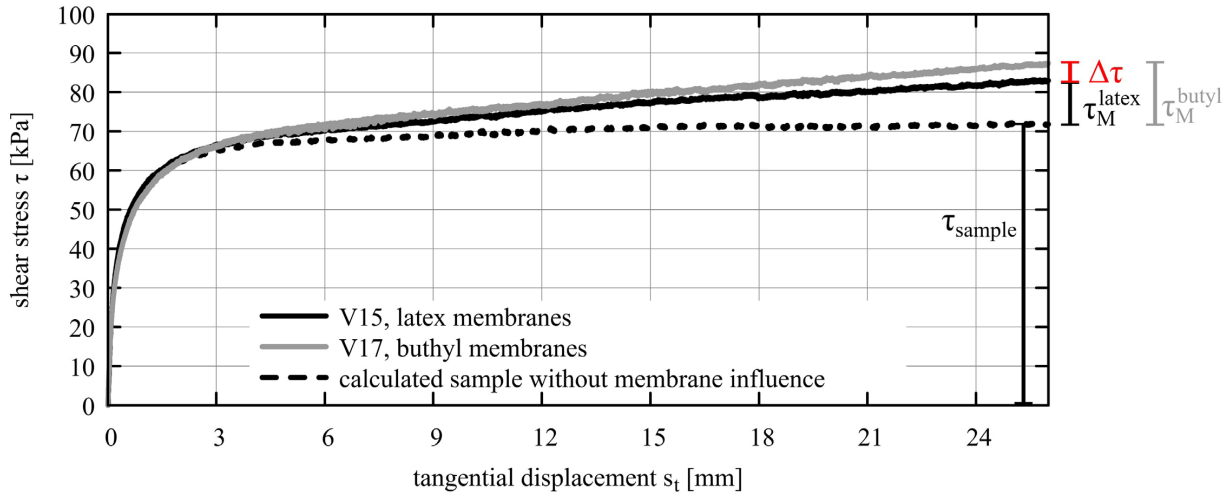


**Figure 6.** Test results of experiment V15 and V17 with different membrane types to develop a correction for the membrane stiffness.

$$\frac{\tau_M^{\text{butyl}}}{\tau_M^{\text{latex}}} = \frac{t_{\text{butyl}} E_{\text{butyl}} \left(r_o^3 + r_i^3\right)\theta}{\left(r_o^3 - r_i^3\right)h}$$
$$\frac{\left(r_o^3 - r_i^3\right)h}{t_{\text{latex}} E_{\text{latex}} \left(r_o^3 + r_i^3\right)\theta} = \frac{t_{\text{butyl}} E_{\text{butyl}}}{t_{\text{latex}} E_{\text{latex}}} \tag{15}$$

From the test results, only the difference of the total global measured shear stress can be calculated:

$$\tau_{\text{tot}}^{V17} - \tau_{\text{tot}}^{V15} = \Delta\tau \tag{16}$$

But with the assumption, that the measured shear stress contributed by the samples shear strength is the same for both tests, the calculated difference $\Delta\tau$ results only from the difference in the membrane stresses:

$$\tau_{\text{tot}}^{V17} - \tau_{\text{tot}}^{V15} = \Delta\tau = \tau_M^{\text{butyl}} - \tau_M^{\text{latex}} \tag{17}$$

There are still two unknown variables in Equation 17. To find their values, the equation is first expanded with a ratio:

$$\Delta\tau = \tau_M^{\text{butyl}} - \tau_M^{\text{latex}} = \frac{\tau_M^{\text{butyl}} \tau_M^{\text{latex}}}{\tau_M^{\text{latex}}} - \tau_M^{\text{latex}} \tag{18}$$

Now, it can be reduced to one unknown variable together with Equation 15:

$$\Delta\tau = \frac{t_{\text{butyl}} E_{\text{butyl}}}{t_{\text{latex}} E_{\text{latex}}} \tau_M^{\text{latex}} - \tau_M^{\text{latex}} \tag{19}$$

The additional measured shear stress induced by the membrane deformation in test V15 with the latex membrane can be calculated with:

$$\tau_M^{\text{latex}} = \frac{\Delta\tau}{\frac{t_{\text{butyl}} E_{\text{butyl}}}{t_{\text{latex}} E_{\text{latex}}} - 1} \tag{20}$$

The correction function is developed from the additional global shear stress induced from the latex membrane at the end of the test. The current global shear stress induced by the membrane is calculated as a proportional function of the rotation angle $\theta$ or the tangential shear displacement $s_t$. To address varying membrane thickness and stiffness, the correction can be adapted to the actual membrane thickness $t_M$ and stiffness $E_M$:

$$\tau_M^{\text{latex}} = 0.389 \frac{\text{kPa}}{\text{mm}} \cdot \frac{t_M E_M}{0.55\,\text{mm} \cdot 1387\ \text{kPa}} s_t \text{ or}$$
$$\tau_M^{\text{latex}} = 0.272 \frac{\text{kPa}}{^\circ} \cdot \frac{t_M E_M}{0.55\,\text{mm} \cdot 1387\ \text{kPa}} \theta \tag{21}$$

This correction can be used for similar geometries and a rotation angle up to 40° and is applied to all tests presented here.

### 3.2 Influence of different stress states – tests with mode A (long samples)

With the membrane correction (Section 3.1) it is possible to determine the contact shear behavior at various stress states. Two representative tests in mode A (long sample) with contact plates with two different roughness properties are displayed in Figure 7. The evolution of the global shear

stress $\tau_{\theta z}$ of both tests is monotonic increasing and tends to an asymptotic value. V30 with a smooth plate (K11) reaches a lower maximum shear stress, then V02 with a rough plate (K0). The maximum shear stress of V30 with the smooth plate is reached at a larger displacement. This matches the findings in the literature for direct interface shear tests, that the contact shear strength increases with the roughness of the contact plate (e.g., Kishida & Uesugi, 1987; Martinez & Stutz, 2019) and will be discussed further in Section 3.5. In direct interface tests, the shear plane is forced to the horizontal plane by the test setup and the stress vector on the contact plane with normal stress $\sigma_N$ and shear stress $\tau$ is analyzed. Whether this approach to analyze only the stress vector on the contact plane is suitable for the novel test method will be discussed along with the experimental results shown in Figure 8, as well as the implications for the description of the in situ behavior. Additionally, the fact that there is more fluctuation in the values of V30 than of V02 (Figure 7) will be discussed in Section 3.3.

Figure 8 displays the shear phase (torsion) of the test series A01:K11 and A02:K0. The graphs in Figure 8a and c belong to test series A01:K11 with a smooth contact plate, the graphs in Figure 8b and d belong to test series A02:K0 with a rough contact plate. The graphs a and b show the deviator stress $q$ (light-colored) and the shear stress on the horizontal plane $\tau_{\theta z}$ (black lines) over the effective mean pressure $p'$.

During the shear phase, the mean effective pressure is constant because of the constant controlled normal stresses $\sigma_z$, $\sigma_r$ and $\sigma_\theta$. The deviator stress $q$ and the horizontal shear stress $\tau_{\theta z}$ increases during the rotation of the bottom plate. The black crosses represent the critical deviator stress calculated with the Mohr-Coulomb model. In the Mohr-Coulomb model, the critical deviator stress $q_{crit}$ depends not solely on the mean effective pressure $p'$ but also on the Lode angle $\theta$ (see the graphs of the deviatoric plane in Figure 8c and d). The value $\theta = 0°$ for the Lode angle is defined as the triaxial compression (the two smallest principal stresses are equal). For the tests with an isotropic initial stress state ($p' = 100$ kPa) the Lode angle $\theta$ is constant during the shearing phase with $\theta = 30°$. For the tests with smaller lateral stresses ($p' = 67$ kPa), the initial state is triaxial compression with $\theta = 0°$ and during the shear phase the Lode angle $\theta$ increases. For the tests with larger lateral stresses ($p' = 133$ kPa) the Lode angle increases from an initial value of $\theta = 60°$. From the comparison of Figure 8a and b it can be noticed, that for the contact plate with a smaller roughness (K11, left hand side) the maximum deviator stress $q$ of the test with $p' = 67$ kPa (V26) reaches the calculated critical deviator stress $q_{crit}$, while the other two ones have a lower maximum deviator stress $q$, than the calculated $q_{crit}$. For the contact plate with a larger roughness (K0, right hand side) the deviator stress reaches the calculated $q_{crit}$ for the tests with V32 ($p' = 67$ kPa) and V02 ($p' = 100$ kPa) while V31 with $p = 133$ kPa has a lower maximum deviator stress $q$, than the calculated $q_{crit}$.

The stress ratio $M = \frac{q}{p'}$ represents the ratio $\tau / \sigma_N$ of the stress vector on the plane, where the $\tau / \sigma_N$-ratio is the largest one. In a pure soil sample this would be the ratio leading to a failure if it exceeds the strength of the sample and the failure would happen in the corresponding plane. For the shear stress on the horizontal plane $\tau_{\theta z}$ displayed in Figure 8a and b the following observation can be made: The shear stress $\tau_{\theta z}$ for the tests with $p' = 67$ kPa – where $q$ reaches $q_{crit}$ – is markable lower than in the other tests. In all tests the normal stress on the contact plane is similar ($\sigma_z = 100$ kPa), hence the absolute shear stress $\tau_{\theta z}$ represents also the $\tau_{\theta z} / \sigma_z$-ratio in the horizontal plane. This ratio is decisive for a failure in the (horizontal) contact plane. Such a failure would occur, if the contact shear strength in an interface would be exceeded or the failure would be forced to the contact plane (e.g. in direct shear tests).

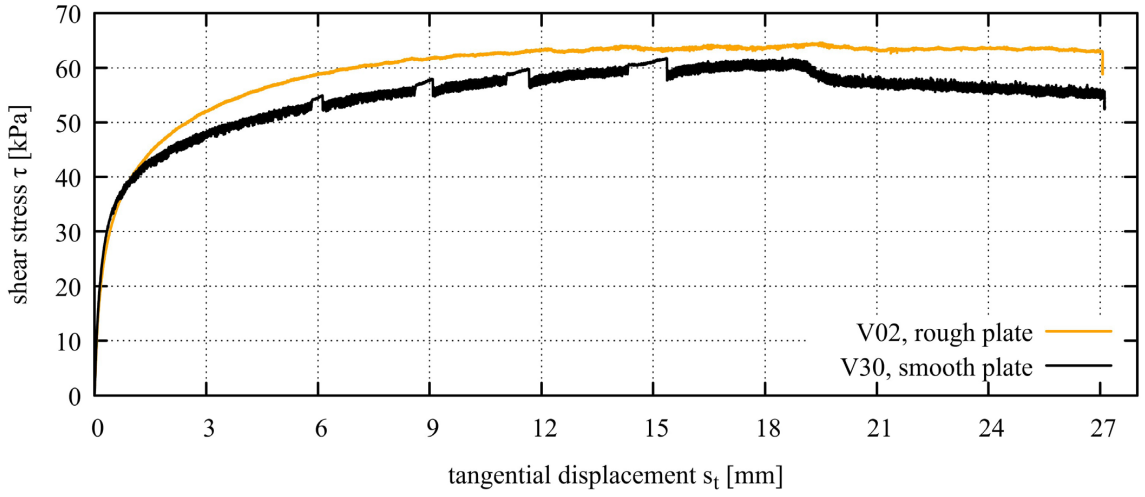


**Figure 7.** Comparison between a smooth (K11) and a rough (K0) top plate. Tests with isotropic initial stress states $\sigma'_z = \sigma'_r = \sigma'_\theta = p' = 100$ kPa.

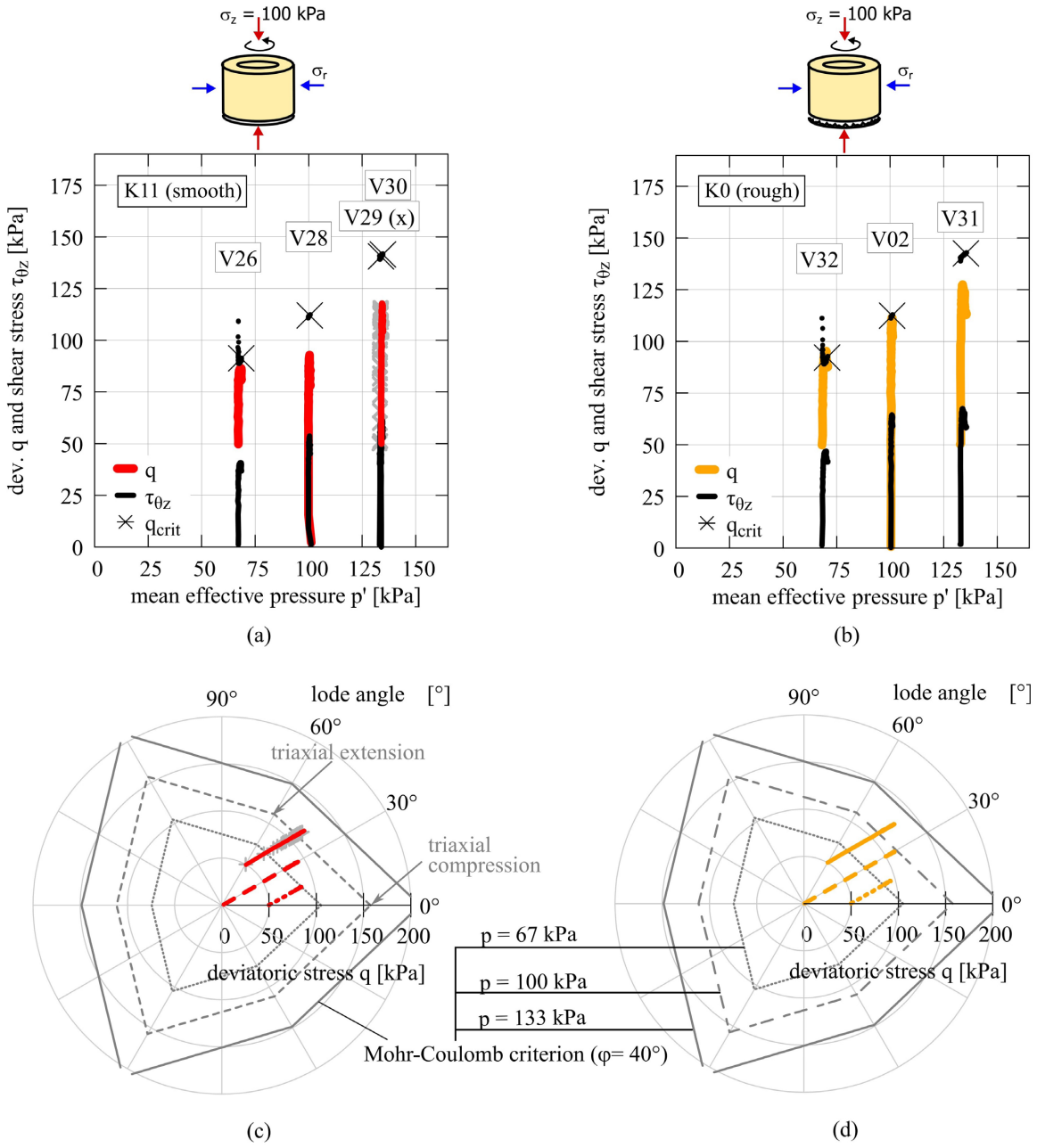


**Figure 8.** Tests in mode A (long sample). (a) and (c) test series A01:K11 (smooth plate), (b) and (d) test series A02:K0 (rough plate).

As a hypothesis, the failure mechanism in the interface tests in the modified hollow cylinder triaxial device is variable, so the failure will occur either in the soil or at the interface. In the soil, the failure will occur on the plane with the maximum ratio $\tau / \sigma_N$ (if it exceeds the soil strength). In the horizontal contact plane, the $\tau / \sigma_N$-ratio is less, but the shear strength (=contact shear strength) is also less. If the shear stress on the contact plane reaches the contact shear strength first, the failure will happen in the contact plane.

For a smoother contact plate, the failure is more likely to happen in the horizontal contact plane. This can be observed using the results of test series A01:K11 and A02:K0: For test series A01:K11 with a smooth contact plate, the test V26 matches the calculated deviator stress from the Mohr-Coulomb criterion (failure in soil is decisive), while the other tests deviate from it (failure on interface plane is decisive). For the test series with the rough endplate (A02:K0), only the test V31 does not match the calculated deviator stress (failure on interface plane is decisive). For the test with $p' = 100\,\text{kPa}$, $q$ matches $q_{crit}$, but the shear stress $\tau_{\theta z}$ is not less than in the test with $p' = 133\,\text{kPa}$. It is likely, that in this test V31 both failure criteria were reached nearly at the same time.

Tests V29 (gray crosses) and V30 (line type as V26 and V28) are repetition tests to check the repeatability of the test results. The test results indicate a high reproducibility.

In a next step, different modeling methods for interface shear behavior can be tested and validated with the experimental results. From the experimental findings, two methods are proposed: 1) Use a relationship between the stress components on the contact plane ($\tau$ -$\sigma_N$) for the interface and a neighboring (maybe extra small) element with the soil model to simulate a failure in the soil ($q_{crit}$). 2) Use an interface model including a dual yield function to model the failure in the contact plane and in an arbitrary plane in the soil at ones.

Both methods might capture the strength by the maximum horizontal shear stress or deviator stress. Another important aspect is dilation, which also affects the evolution of strength. The dilation in soil-structure interaction is influenced by the roughness of the contact surface and therefore might not be solely captured with a neighboring soil element.

### 3.3 Sliding and shearing at the contact

In the used test device, the torsional deformation of the sample is measured by the displacement of the top plate against the bottom plate. With this measurement, only the global deformation of the sample can be determined. In element tests, the assumption is taken, that the strain and stress in each position (small element of the sample) is equal and therefore, the stress and strain can be calculated from global measured values. Interface tests in general are no element tests because a concentrated deformation can occur on the interface and the strain near to the contact surface may be greater than far away from it. Hence, the total displacement of the end caps is composed of the shear deformation in the soil (or a part of it) and the sliding between the contact plate and the soil (Niebler et al., 2025).

Figure 7 displays shear stress during tests V02 and V30 with contact plates with different roughness properties. It is noticeable that the scatter of the measured values has a different span for the smooth plate and the rough plate. Also, the span of the scatter is changing during the tests with the smooth end plate. A possible explanation is the slipping and shearing on the interface. For the rough end plate, no sliding occurs - there is a continuous frictional connection with force transmission between the contact plate and the soil. Therefore, the scatter in the shear stress is lower. For the smooth plate, there are alternating sections with higher and lower scatters. This might connect to an alternation between a sliding and a sticking regime at the interface. During phases with much scatter, there is a permanent change in the transferred force with sliding and sticking at the contact plate. The axial displacement and volume change measurements of V02 and V30 displayed in Figure 9 support this hypothesis.

During the phases of V30 with less scatter (connected to a sticking regime), the globally measured volumetric change and axial displacement show a steeper slope (more deformation is happening). This happens at a tangential displacement of approximately 6 mm, 9 mm, 11 mm, and 15 mm. A possible explanation is: During the sticking regime, more grains are mobilized and sheared and produce therefore a larger sum of dilative or contractive deformation which leads to a larger measured axial displacement or volume change.

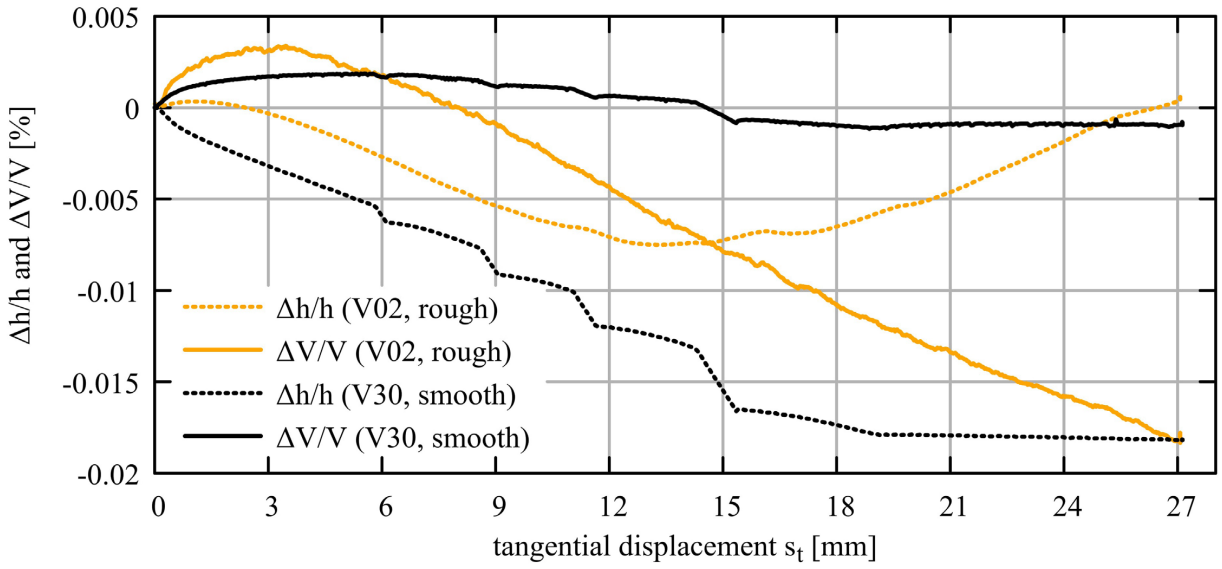


**Figure 9.** Normalized displacements of test V02 (rough contact plate, K0) and V30 (smooth contact plate, K11). The global measured and normalized axial displacement $\Delta h / h$ and volumetric change $\Delta V / V$ are displayed over the shear displacement (tangential displacement $s_t$).

### 3.4 Tests with mode B (short sample)

In this work, a second test mode (mode B) was used in the modified hollow cylinder triaxial device. The difference compared to test mode A with long samples ($h = 100$ mm) is the use of short samples with $h = 20$ mm. The test series B01:K3 with a less rough contact plate and test series B02:K0 with a rough contact plate are presented in Figure 10 and both conducted in mode B (short samples).

It is noticeable that the maximum deviator stress $q$ reached in the tests does not match the calculated critical deviator stress $q_{crit}$ with the Mohr-Coulomb model at the end of the test (marked with the black checkmarks in Figure 10). The deviator stress sometimes reaches not only smaller but even larger values than the calculated $q_{crit}$. This wouldn't be expected for soil element tests. The horizontal shear stress $\tau_{\theta z}$ (black lines) reaches similar values across the tests within each series. For tests V20, V15, V10 and V08, the

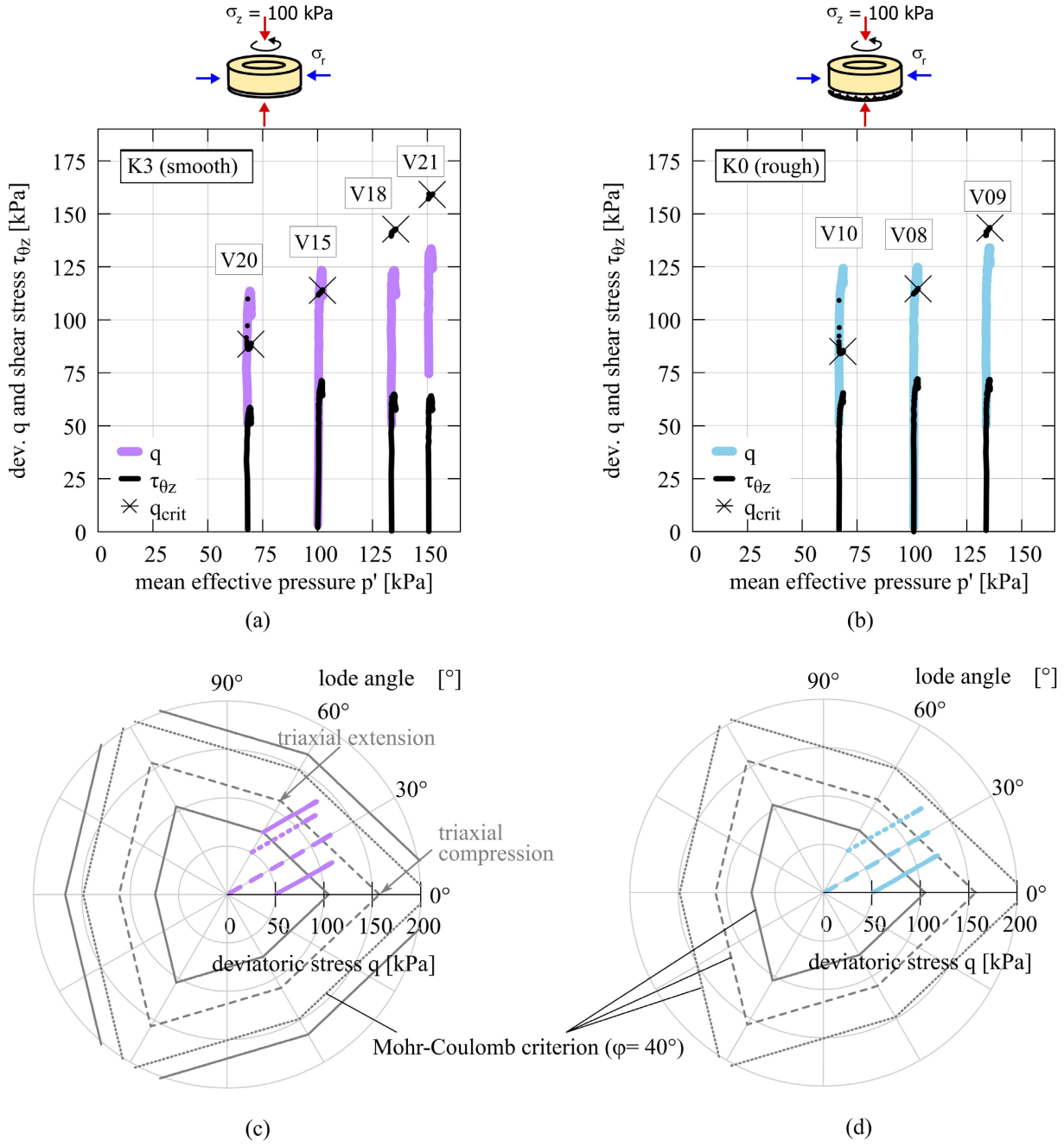


**Figure 10.** Tests in mode B (short sample). (a) and (c) test series B01:K3 with less rough contact plate K3, (b) and (d) test series B02:K0 with rough contact plate K0. Extended based on (Gehring et al., 2024).

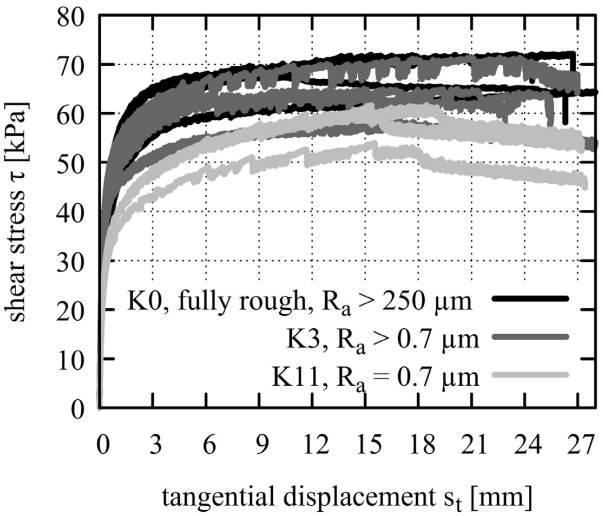


**Figure 11.** Shear stress for tests with horizontal failure plane and contact plates with different roughness properties.

deviator stress is larger than the calculated $q_{crit}$ for failure in the soil. If these tests had been conducted in mode A, a failure would be expected in the soil on the plane with the maximum $\tau / \sigma$ -ratio and the deviator stress would be limited to the calculated $q_{crit}$ (black crosses). This does not occur in these tests conducted in mode B. The different geometry appears to prevent this failure in the soil. This leads to the hypothesis that failure is restricted to the horizontal plane for tests in mode B. The maximum shear stress in the horizontal contact plane is decisive for the failure. It depends only on the normal force on the contact plane, which is equal in all tests in test series B01:K3 and B02:K0 and leads to similar values for the shear stress $\tau_{\theta z}$ across the tests.

### 3.5 Influence of roughness properties of the contact plate

Previous studies have shown that the maximum shear stress increases with an increasing surface roughness (see section 1). For tests in mode A with a long sample, the surface roughness is one of the factors governing the failure mode (see section 3.2). In the present section, tests with failure occurring in the horizontal plane on the contact surface are compared to investigate the influence of surface roughness on the maximum shear stress in the contact plane. Figure 11 displays the shear stress with increasing tangential displacement of the contact plate. The darker the line, the greater the surface roughness $R_a$ of the used contact plate. The tests with a smoother contact plate tend to reach lower maximum shear stress values than those with a rougher contact plate. This is in accordance with the aforementioned findings from the literature. Still, the tests show significant deviations due to the different boundary conditions. Another point should be noted regarding the measured roughness values: The measured surface roughness in three spots is similar for the plate K3 and K11, but the surface of K3 includes two larger filter stones and six screws (12% of the contact area) whereas K11 only contains two smaller filter stones (2% of the contact area). The additional screws contribute to the roughness of the surface and therefore, K3 behaves like a plate with a rougher surface than K11. This is reflected in the test results, as K3 shows higher maximum shear stress values than K11.

## 4. Conclusions

In this work, a novel test method for interface shear tests is presented. For this method and the first test results, the following conclusions can be made.

- With the new test method, four independent stress (or strain) components can be controlled in interface tests. Thereby, the influence of normal stress on the planes orthogonal to the interface can be investigated.
- A correction function for membrane stiffness was developed to correct the measured torque taking the deformation mode in the presented tests into account.
- For samples tested in mode A (long sample), as a hypothesis, the failure occurs either in the soil or on the contact plane. If it fails in the soil, the failure plane is the plane with the stress vector with the maximum ratio $\tau / \sigma_N$ of shear stress and normal stress. On the contact plane, the shear-stress-normal-stress ration is less, but also the strength is less on this plane: only the interface friction angle acts there.
- For samples tested in mode B (short sample), the failure in the soil is prevented by the geometry and therefore the failure plane is restricted to the horizontal contact plane.

## Acknowledgments

This work benefits from the student research of Philipp Förschler and Tabea Lohrmann.

## Declaration of interest

The authors have no conflicts of interest to declare. All co-authors have observed and affirmed the contents of the paper and there is no financial interest to report.

## Authors' contributions

Sabine Gehring: conceptualization, data curation, formal analysis, investigation, visualization, writing – original draft. Hans Henning Stutz: conceptualization, resources, supervision, writing – review and editing.

## Data availability

The data sets generated are available from the corresponding author upon reasonable request.

## Declaration of use of generative artificial intelligence

This work was prepared with the assistance of generative artificial intelligence (Writefull and QuillBot) with the aim to enhance the linguistic quality of the text. The entire process of using this tool was supervised, reviewed and when necessary edited by the authors. The authors assume full responsibility for the content of the publication that involved the aid of GenAI.

## List of symbols and abbreviations

| | |
|---|---|
| $b$ | coefficient for the ratio of the principal stresses |
| $d_i$ | inner diameter of hollow cylinder sample |
| $d_o$ | outer diameter of hollow cylinder sample |
| $e_0$ | void ratio after sample preparation |
| $e_{\min}$ | minimum void ratio, estimated in laboratory tests following DIN 18126:2022-10 |
| $e_{\max}$ | maximum void ratio, estimated in laboratory tests following DIN 18126:2022-10 |
| $h$ | sample height |
| $p'$ | mean effective stress |
| $p_i$ | inner cell pressure |
| $p_o$ | outer cell pressure |
| $q$ | deviator stress |
| $q_{\text{crit}}$ | critical deviator stress (calculated with Mohr-Coulomb model from mean effective stress $p$ and Lode angle $\theta$) |
| $r_i$ | inner radius of sample |
| $r_o$ | outer radius of sample |
| $s_t$ | tangential displacement, displacement of a point on the medium circumference of the bottom plate of the sample along the medium circumference, represents shear displacement |
| $t_{\text{butyl}}$ | thickness of butyl membranes in test V17 |
| $t_{\text{latex}}$ | thickness of latex membranes in test V15 |
| $t_M$ | thickness of membranes |
| $u_{\text{so}}$ | displacement due to shearing of soil (sticking of contact plate) |
| $u_{\text{str}}$ | displacement due to sliding between soil and contact surface |
| $CLA$ | center line average |
| $E_{\text{butyl}}$ | stiffness of butyl membranes in test V17 |
| $E_{\text{latex}}$ | stiffness of latex membranes in test V15 |
| $E_M$ | stiffness of membranes |
| $F_{ax}$ | axial force in the test device |
| $I_d$ | relative density |
| $M_{crit}$ | critical stress ratio |
| $M_t$ | measured moment due to torsion in the test device |
| $R_a$ | average roughness, average deviation from mean line of surface |
| $\varepsilon_{\text{vol}}$ | global measured volumetric strain of the sample |
| $\theta$ | rotation angle of bottom plate |
| $\theta$ | lode angle (roscoe invariant) |
| $\rho_s$ | grain density |
| $\sigma_1, \sigma_2, \sigma_3$ | principal stresses |
| $\sigma_{ij}$ | stress tensor |
| $\sigma_N$ | normal stress component of stress vector on specific plane in sample |
| $\sigma_{\text{OP},1}$ , $\sigma_{\text{OP},2}$ | normal stress component of stress tensor in sample on orthogonal planes |
| $\sigma_{\text{PP}}$ | normal stress component of stress tensor in sample on parallel plane |
| $\sigma_r$ | radial stress |
| $\sigma_z$ | vertical stress |
| $\sigma_\theta$ | tangential stress |
| $\tau$ | shear stress component of stress vector on specific plane in sample |
| $\tau_M$ | additional global measured shear stress due to the membrane stiffness |
| $\tau_M^{\text{butyl}}$ | additional global measured shear stress due to the stiffness of the butyl membrane in test V17 |
| $\tau_M^{\text{latex}}$ | additional global measured shear stress due to the stiffness of the latex membrane in test V15 |
| $\tau_{\text{tot}}^{V15}$ | total global measured shear stress in test V15 |
| $\tau_{\text{tot}}^{V17}$ | total global measured shear stress in test V17 |
| $\tau_{\theta z}$ | shear stress in the horizontal plane of the sample |
| $\varphi$ | friction angle |
| $\varphi_r$ | contact friction angle |
| $\Delta\tau$ | difference of global measured shear stress in V17 and V15 |

## References


Arnold, M., & Herle, I. (2006). Hypoplastic description of the frictional behaviour of contacts. *Numerical Methods in Geotechnical Engineering*, *1*, 101-106.

Broms, B.B., & Casbarian, A.O. (1965). Effect of rotation of the principal stress axes and of the intermediate principal stress on the shear strength. *Proceedings 6th ICSMFE*, *1*, 179–183.

Corfdir, A., Lerat, P., & Vardoulakis, I. (2004). A cylinder shear apparatus. *Geotechnical Testing Journal*, *27*(5), 447-455. https://doi.org/10.1520/GTJ11551.

DeJong, J.T., White, D.J., & Randolph, M.F. (2006). Microscale observation and modeling of soil-structure interface behavior using particle image velocimetry. *Soil and Foundation*, *46*(1), 15-28. https://doi.org/10.3208/sandf.46.15.

Frost, J.D., & Han, J. (1999). Behavior of interfaces between fiber-reinforced polymers and sands. *Journal of Geotechnical and Geoenvironmental Engineering*, *125*(8), 633-640. https://doi.org/10.1061/(ASCE)1090-0241(1999)125:8(633).

Gehring, S., Niemunis, A., & Stutz, H.H. (2023). The anisotropic preconsolidation of clay in modelling soil-structure-interface behaviour. In L. Zdravkovic, S. Kontoe, D.M.G. Taborda & A. Tsiampousi (Eds.), *Proceedings 10th NUMGE 2023*. London: ISSMGE. https://doi.org/10.53243/NUMGE2023-120.

Gehring, S., Stutz, H.H., Lohrmann, T., & Förschler, P. (2024). Influence of lateral stress on soil-structure interface tests in a hollow cylinder apparatus. In N. Guerra, M. M. Fernandes, C. Ferreira, A. G. Correia, A. Pinto & P. S. Pinto (Eds.), *Geotechnical engineering challenges to meet current and emerging needs of society* (pp. 1640-1643). London: CRC Press. https://doi.org/10.1201/9781003431749-304.

Hight, D.W., Gens, A., & Symes, M.J. (1983). The development of a new hollow cylinder apparatus for investigating the effects of principal stress rotation in soils. *Geotechnique*, *33*(4), 355-383. https://doi.org/10.1680/geot.1983.33.4.355.

Ghionna, V.N., & Mortara, G. (2002). An elastoplastic model for sand–structure interface behaviour. *Geotechnique*, *52*(1), 41-50. https://doi.org/10.1680/geot.2002.52.1.41.

Jardine, R.J., Lehane, B.M., & Everton, S.J. (1993). Friction coefficients for piles in sands and silts. In D.A. Ardus, D. Clare, A. Hill, R. Hobbs, R.J. Jardine & J.M. Squire (Eds.), *Offshore Site Investigation and Foundation Behaviour: Papers presented at a conference organized by the Society for Underwater Technology and held in London* (pp. 661-677). Dordrecht: Springer Netherlands. https://doi.org/10.1007/978-94-017-2473-9_31.

Kishida, H.L., & Uesugi, M. (1987). Tests of the interface between sand and steel in the simple shear apparatus. *Geotechnique*, *37*(1), 45-52. https://doi.org/10.1680/geot.1987.37.1.45.

Kiyota, T., Sato, T., Koseki, J., & Abadimarand, M. (2008). Behavior of liquefied sands under extremely large strain levels in cyclic torsional shear tests. *Soil and Foundation*, *48*(5), 727-739. https://doi.org/10.3208/sandf.48.727.

Konkol, J. (9-13 June, 2025). Rate-dependent shear behaviour of silt-steel and sand-steel interfaces. In *Proceedings of ISFOG 2025, 5th International Symposium of Frontiers in Offshore Geotechnics*, Nantes, France. https://doi.org/10.53243/ISFOG2025-541.

Koseki, J., Yoshida, T., & Sato, T. (2005). Liquefaction properties of Toyoura sand in cyclic tortional shear tests under low confining stress. *Jiban Kogakkai Ronbun Hokokushu*, *45*(5), 103-113. https://doi.org/10.3208/sandf.45.5_103.

Lemos, L.J.L., & Vaughan, P.R. (2000). Clay–interface shear resistance. *Geotechnique*, *50*(1), 55-64. https://doi.org/10.1680/geot.2000.50.1.55.

Liu, S.A., Liao, C., Su, X., Chen, J., & Xia, X. (2024). Shear rate and roughness effect on clay-steel interface strength properties in CU and CPD drainage conditions. *Ocean Engineering*, *305*, 117956. https://doi.org/10.1016/j.oceaneng.2024.117956.

Martinez, A., & Stutz, H.H. (2019). Rate effects on the interface shear behaviour of normally and overconsolidated clay. *Geotechnique*, *69*(9), 801-815. https://doi.org/10.1680/jgeot.17.P.311.

Meier, A.L., Faro, V.P., & Odebrecht, E. (2023). Shear strength analysis of interfaces between granular soils and concrete cured under stress. *Soils and Rocks*, *46*(1), e2023004022. https://doi.org/10.28927/SR.2023.004022.

Niebler, M., Chrisopoulos, S., Cudmani, R., & Rebstock, D. (2025). A general framework to simulate soil–structure interface behaviour using advanced constitutive models. *Modelling*, *6*(1), 11. https://doi.org/10.3390/modelling6010011.

Potyondy, J.G. (1961). Skin friction between various soils and construction materials. *Geotechnique*, *11*(4), 339-353. https://doi.org/10.1680/geot.1961.11.4.339.

Saada, A.S. (1988). Hollow cylinder torsional devices: their advantages and limitations. *Advanced Triaxial Testing of Soil and Rock*, *977*, 766-789. https://doi.org/10.1520/STP29113S.

Staubach, P., Machaček, J., & Wichtmann, T. (2022). Novel approach to apply existing constitutive soil models to the modelling of interfaces. *International Journal for Numerical and Analytical Methods in Geomechanics*, *46*(7), 1241-1271. https://doi.org/10.1002/nag.3344.

Stutz, H., Wuttke, F., & Benz, T. (2014). Extended zero-thickness interface element for accurate soil–pile interaction modelling. In M.A. Hicks, R.B.J. Brinkgreve & A. Rohe (Eds.), *Numerical methods in geotechnical engineering, hicks, brinkgreve & royce* (pp. 283-288). London: Taylor & Francis Group. https://doi.org/10.1201/b17017-52.

Stutz, H., Mašín, D., Sattari, A.S., & Wuttke, F. (2017). A general approach to model interfaces using existing soil constitutive models application to hypoplasticity. *Computers and Geotechnics*, *87*, 115-127. https://doi.org/10.1016/j.compgeo.2017.02.010.

Stutz, H.H., Doose, R., & Wuttke, F. (2018). Open science interface shear device. In *Proceedings of China-Europe Conference on Geotechnical Engineering: Volume 1* (pp. 615-618). Cham: Springer International Publishing. https://doi.org/10.1007/978-3-319-97112-4_137.

Stutz, H.H., & Martinez, A. (2021). Directionally dependent strength and dilatancy behavior of soil–structure interfaces. *Acta Geotechnica*, *16*(9), 2805-2820. https://doi.org/10.1007/s11440-021-01199-5.

Tejchman, J., & Wu, W. (1995). Experimental and numerical study of sand–steel interfaces. *International Journal for Numerical and Analytical Methods in Geomechanics*, *19*(8), 513-536. https://doi.org/10.1002/nag.1610190803.

Uesugi, M., & Kishida, H. (1986). Frictional resistance at yield between dry sand and mild steel. *Soil and Foundation*, *26*(4), 139-149. https://doi.org/10.3208/sandf1972.26.4_139.

Wernick, E. (1978). *Heft Nr. 75: Tragfähigkeit zylindrischer Anker in Sand unter besonderer Berücksichtigung des Dilatanzverhaltens* [Doctoral thesis]. Karlsruhe Institute of Technology.

Wichtmann, T., & Triantafyllidis, T. (2016). An experimental database for the development, calibration, and verification of constitutive models for sand with focus to cyclic loading: part I—tests with monotonic loading and stress cycles. *Acta Geotechnica*, *11*(4), 739-761. https://doi.org/10.1007/s11440-015-0402-z.